$Ce_{1-x}Y(Nd)_xO_{2-\delta}$ nanopowders: potential materials for intermediate temperature solid oxide fuel cells

2006 J. Phys.: Condens. Matter 18 S2061

(http://iopscience.iop.org/0953-8984/18/33/S22)

INSTITUTE OF PHYSICS PUBLISHING JOURNAL OF PHYSICS: CONDENSED MATTER

J. Phys.: Condens. Matter **18** (2006) S2061–S2068 doi:10.1088/0953-8984/18/33/S22

$Ce_{1-x}Y(Nd)_xO_{2-\delta}$ nanopowders: potential materials for intermediate temperature solid oxide fuel cells

Z D Dohčević-Mitrović[1], M Grujić-Brojčin[1], M Šćepanović[1], Z V Popović[1], S Bošković[2], B Matović[2], M Zinkevich[3] and F Aldinger[3]

[1] Centre for Solid State Physics and New Materials, Institute of Physics, Pregrevica 118, 11080 Belgrade, Serbia
[2] Institute of Nuclear Sciences 'Vinča', 11001 Belgrade, Serbia
[3] Max-Planck Institute für Metallforschung, 70569 Stuttgart, Heisenbergstrasse 1, Germany

E-mail: zordoh@phy.bg.ac.yu

Received 16 January 2006, in final form 8 March 2006
Published 4 August 2006
Online at stacks.iop.org/JPhysCM/18/S2061

Abstract

Nanopowdered solid solution $Ce_{1-x}Y(Nd)_xO_{2-\delta}$ samples ($0.1 \leqslant x \leqslant 0.25$) were made by self-propagating room temperature (SPRT) synthesis. The first-order Raman spectra of $Ce_{1-x}Y(Nd)_xO_{2-\delta}$ samples measured at room temperature exhibit three broad features: the main Raman active F_{2g} mode at about 450 cm^{-1} and two broad features at about 550 (545) and 600 cm^{-1}. The mode at ~600 cm^{-1} was assigned to the intrinsic oxygen vacancies due to the nonstoichiometry of ceria nanopowders. The mode at about 550 (545) cm^{-1} was attributed to the oxygen vacancies introduced into the ceria lattice whenever Ce^{4+} ions are replaced with trivalent cations (Y^{3+}, Nd^{3+}). The intensity of this mode increases with doping in both series of samples, indicating a change of O^{2-} vacancy concentration. The mode frequency shifts in opposite direction in Y- and Nd-doped samples with doping level, suggesting that different types of defect space can occur in Y- and Nd-doped ceria nanopowders.

1. Introduction

Solid oxide fuel cells (SOFCs) are electrochemical devices which combine hydrogen fuel with oxygen to produce electric power, heat and water. SOFCs usually consist of three main components: anode, cathode and electrolyte layers. The main focus of investigation is aimed at the optimization of SOFCs to operate at reduced temperatures (<500 °C) thus enabling the use of less costly materials for the cell interconnect and system components. This optimization can be performed with the use of new electrolyte materials having high ionic conductivity and low electronic conductivity at moderate temperatures. Ceria-based electrolytes offer many advantages (notably higher conductivities at lower operating temperatures and compatibility with high performance cathode materials) over traditional zirconia-based electrolytes that

require a high temperature (>1273 K) for the onset of ionic conductivity [1–5]. Nanosized ceria (CeO_2) doped with oxides of di- or trivalent metals is a promising solid electrolyte with excellent ionic conductivity at low temperature: partial replacement of Ce^{4+} ions with di- or trivalent rare earth ions produces a large density of oxygen vacancies in the ceria lattice, enhancing the conductivity of these materials [6–8].

The purpose of this work was to show that ceria nanopowders doped with trivalent (Y, Nd) cations over the range $0.1 \leqslant x \leqslant 0.25$, fabricated by a simple and cost-effective self-propagating room temperature synthesis (SPRT) method, can be used as a potential electrolyte material in SOFC applications. We focused our attention on the concentration ranges of each dopant for which solid solutions with a fluorite structure of CeO_2 are obtained. The samples were studied by Raman scattering, x-ray diffraction (XRD) and scanning electron microscope (SEM) methods. Raman spectroscopy at room temperature was used to identify and distinguish the increasing concentration of intrinsic and extrinsic oxygen vacancies in doped nanopowder samples since XRD is almost insensitive to the concentration of O vacancies.

2. Experimental aspects

The solid solutions of yttrium- and neodymium-doped samples were prepared by a SPRT method using metal nitrates and sodium hydroxide as the starting materials [9]. Preparation of $Ce_{1-x}Y(Nd)_xO_{2-\delta}$ powders was performed by hand mixing chemicals according to:

$$2[(1-x)Ce(NO_3)_3{\cdot}6H_2O + xMe(NO_3)_3{\cdot}6H_2O] + 6NaOH + (\tfrac{1}{2} - \delta)O_2 \rightarrow 2Ce_{1-x}Me_xO_{2-\delta} + 6NaNO_3 + 15H_2O. \quad (1)$$

The compositions of the reacting mixtures were calculated according to the nominal composition of the final reaction product. Compositions of $Ce_{1-x}Y(Nd)_xO_{2-\delta}$ were synthesized with x ranging from 0 to 0.25. The described reaction belongs to a group of double exchange reactions, and develops spontaneously after being initiated, coming to an end extremely rapidly. After the mixture of reactants was mechanically activated (by hand mixing instead by heating) the reaction took place at room temperature and terminated very quickly. The obtained mixtures of reaction products according to (1) were subjected to centrifuge treatment to eliminate $NaNO_3$. After drying, the structure of the solid solutions was identified by means of powder XRD on a Siemens D-5000 XRD diffractometer with Cu Kα radiation at room temperature. The average grain size was measured from the (111) XRD peak using the Scherrer formula. SEM analysis using Zeiss DSM 982 Gemini scanning electron microscope proved that the obtained powders were in the nanometric size range.

The Raman spectra were obtained using a U-1000 (Jobin-Ivon) double monochromator in the backscattering geometry. The Raman spectra were excited by the 488 nm line of an Ar^+ ion laser and taken at room temperature. In order to avoid sample heating we used a line focus and the laser power was kept lower than 100 mW.

3. Results and discussion

XRD results for Y- and Nd-doped samples, summarized in a recent publication [9], appeared to be single phase for the whole doping range retaining the CeO_2 fluorite structure. Diffraction lines of starting oxides Y_2O_3 and Nd_2O_3 are not registered in the whole doping range. The XRD patterns for two doped samples, $Ce_{0.75}Y_{0.25}O_{2-\delta}$ and $Ce_{0.75}Nd_{0.25}O_{2-\delta}$, are shown in figure 1.

The standard XRD pattern of $CeO_{2-\delta}$ nanopowder is also illustrated for comparison. The broadened XRD peaks suggest that the particles are within the nanometre scale with an average

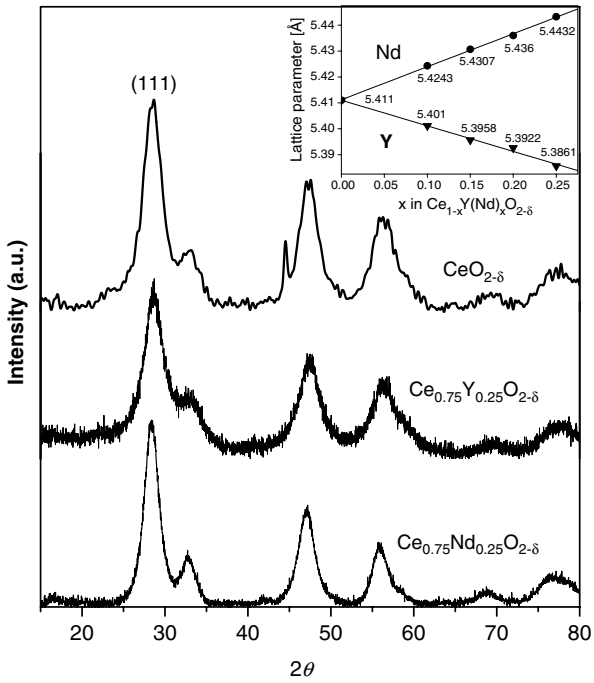

Figure 1. X-ray diffraction pattern of $Ce_{0.75}Y(Nd)_{0.25}O_{2-\delta}$, nanopowdered samples. Pure $CeO_{2-\delta}$ nanopowder is presented as the reference sample. Inset: the lattice parameter change in $Ce_{1-x}Y(Nd)_xO_{2-\delta}$ nanopowders.

crystallite size of between 4 and 6 nm [9]. The change in lattice parameter against the dopant concentration is plotted in the inset of figure 1. The change in the lattice constant in doped samples is directly correlated with the ionic size of the dopants: larger Nd dopants dilate while the smaller Y dopants contract the lattice, obeying Vegard's law. From the change in lattice parameter of pure and doped ceria samples, and bearing in mind Tsunekawa's work about the dependence of the lattice parameter on crystalline size in ceria nanoparticles [10], we assumed that there are no compositional and structural changes from CeO_2 to C-type sesquioxide, Ce_2O_3, usually formed in small ceria nanoparticles. On the other hand, Zhou and co-workers showed [11] that the formation of the defects on the lattice, especially oxygen vacancies, can induce lattice relaxation in ceria nanopowders.

SEM images of $Ce_{0.75}Y_{0.25}O_{2-\delta}$ and $Ce_{0.75}Nd_{0.25}O_{2-\delta}$ powder samples are shown in figures 2(a) and (b), while the particle size distribution (PSD) derived from a SEM photograph of $Ce_{0.75}Nd_{0.25}O_{2-\delta}$ is presented in figure 2(c). SEM images show that the particle diameters of both series of samples are in a narrow range with a PSD maximum centred on 10 nm. The discrepancy between XRD [9] and SEM results could be due to the fact that XRD method allows us to determine an average size of the individual crystallites (Scherrer formula) whereas the SEM images reflect the dimension of whole agglomerated particle composed of a few nanocrystallites.

Room-temperature first-order Raman spectra of the nanostructured ceria samples doped with yttrium and neodymium show a strong peak at $\sim$454 cm^{-1} corresponding to the triply degenerate F_{2g} mode of fluorite CeO_2 structure [12, 13]. This mode has a strong shift to lower energies in comparison with its bulk counterpart, increasing linewidth with pronounced

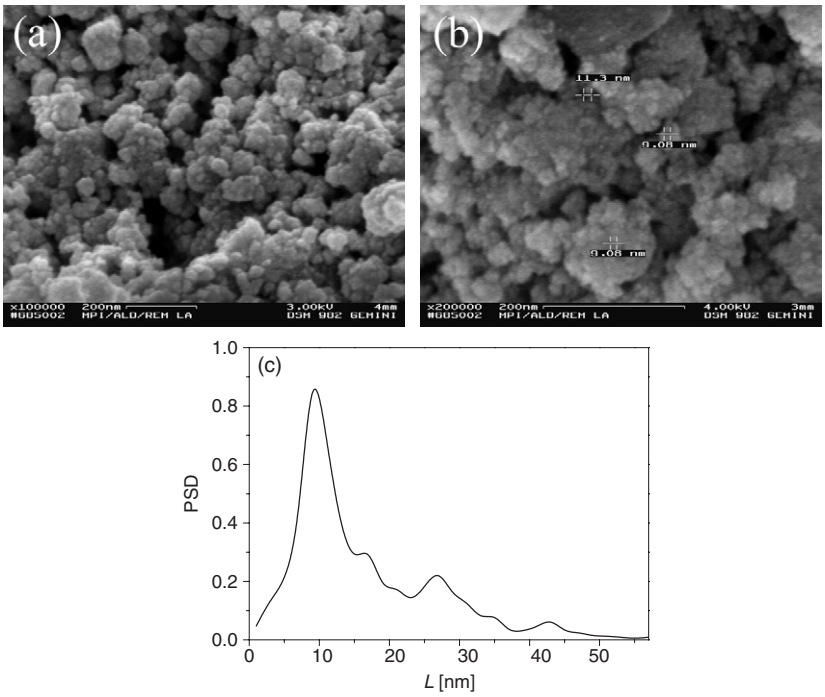

Figure 2. SEM images of (a) $Ce_{0.75}Y_{0.25}O_{2-\delta}$ and (b) $Ce_{0.75}Nd_{0.25}O_{2-\delta}$ samples together with the particle size distribution function (PSD) obtained from SEM image of an $Ce_{0.75}Nd_{0.25}O_{2-\delta}$ sample (c).

asymmetry on the low-energy side. In Nd-doped samples there is a systematic, small shift of the F_{2g} mode to lower frequencies (in $Ce_{0.75}Nd_{0.25}O_{2-\delta}$ this mode is positioned at $\sim$450 cm^{-1}) with increasing doping level. In Y-doped samples this mode has a slight blueshift with maximum dopant concentration (1–2 cm^{-1}). In a recent publication [14] we have shown that the strong shift and asymmetric broadening of the Raman F_{2g} in pure and doped ceria samples could be well explained by combined size and inhomogeneous strain effects including the dispersion in particle size that explains the asymmetry of the Raman F_{2g} mode. We have also demonstrated that Richter's [15] and Campbell's [16] confinement models, as well as Spanier's model [17] for average strain, were incapable of explaining our experimental Raman spectra. As well as the inclusion of the effects of inhomogeneous strain we were forced to introduce a different boundary condition for the Gaussian localization function i.e. $\beta \sim 4\pi^2$ for our doped nanopowders. The Raman spectra of Y(Nd)-doped samples are given in figures 3 and 4.

The calculated Raman line shape functions using our proposed model [14] can be written as:

$$I(\omega) = \sum_{1}^{3} \int_{0}^{\infty} F(L) \int_{BZ} \frac{\exp\left(\frac{-q^2L^2}{8\beta}\right) \mathrm{d}^3q}{[\omega - (\omega_i(q) + \Delta\omega_i(q, L))]^2 + (\Gamma_0/2)^2} \mathrm{d}L \qquad (2)$$

and are also presented in figures 3 and 4 with full lines. The best fit was obtained when the average particle size for Y(Nd)-doped ceria nanopowders was taken to be $L_0 = 7$ nm. The effects of inhomogeneous strain are included through the Gaussian size distribution function $F(L)$ centred at the mean grain size L_0. The variable parameter during the fitting procedure, the Gaussian width (w), is also given for each series of samples in figures 3 and 4.

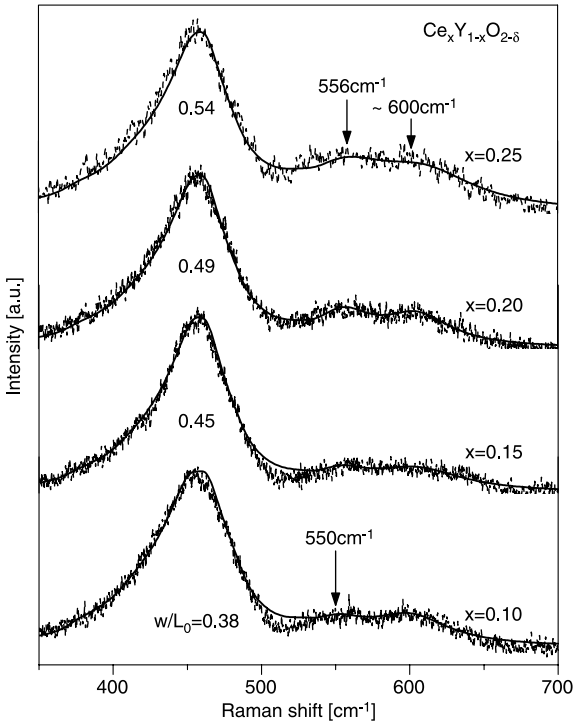

Figure 3. Raman spectra of Y-doped ceria nanopowders (dashed line) together with calculated spectra (full lines) according to the spatial correlation model, equation (2).

The most interesting features of the Raman spectra of Y(Nd)-doped nanopowders is the appearance of two additional Raman modes. The shape of these two modes can be described well by a Lorentzian form, as can be seen from figures 3 and 4. The Raman peak around 600 cm^{-1} is already seen in pure ceria nanopowders [14, 18] and is attributed to the defect spaces which include oxygen vacancies [19, 20]. This intrinsic O^{2-} vacancies originate from increased non-stoichiometry of nanocrystalline ceria powders. In Y- and Nd-doped nanopowdered samples this mode is at almost the same position and its intensity does not vary much with doping level. A new weak shoulder on the high frequency side of the F_{2g} band appears in both series of doped ceria samples. This feature evolves into a broad peak whose intensity tends to increase with increasing Y or Nd content. The position of this mode in Y-doped samples changes from ∼550 cm^{-1} for the lowest Y content to ∼556 cm^{-1} for the highest Y content. In Nd-doped samples this mode appears at lower frequencies changing position from ∼545 to ∼540 cm^{-1} with Nd doping level from 10% to 25%, respectively. The intensity and position of this mode in Y^{3+}- and Nd^{3+}-doped ceria nanopowders are presented in figures 5 and 6.

To the best of our knowledge this mode was found for the first time in the work of Nakajima *et al* regarding the single crystals of Y-doped CeO_2 [13]. They found a pronounced Raman shift of this mode (from 540 to 560 cm^{-1}) upon varying the dopant concentration from $x = 0.09$ to 0.18. Nakajima and co-workers attributed this mode to the defect spaces which include O^{2-} vacancies, while its position changes with different atomic surrounding, i.e. they proposed four kinds of defect space in such a system. The presence of this mode is also evident in the work

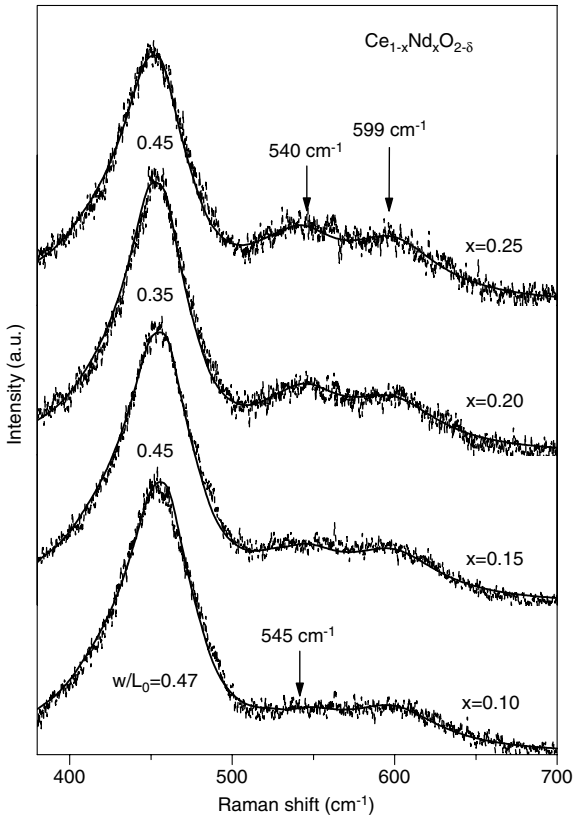

Figure 4. Raman spectra of Nd-doped ceria nanopowders (dashed line) together with calculated spectra (full lines) according to the spatial correlation model, equation (2).

of Lin *et al* [20] in solid solutions of Nd^{3+}-doped CeO_2 with small particle size ∼7.2 nm, but without any explanation for its origin. Having in mind these two papers, we concluded that in our Y- and Nd-doped nanostuctured samples the appearance of a new mode can be ascribed to the oxygen vacancies introduced into the ceria lattice in order to maintain charge neutrality when Ce^{4+} ions are replaced with trivalent cations. The different mode frequency shift in Y- and Nd-doped samples is in accordance with the compression and extension of unit cell parameters by Y and Nd doping (see the inset in figure 1). We also suggest that the mode position is probably influenced by a change in the type of defect space in $Ce_{1-x}Y(Nd)_xO_{2-\delta}$. In Y-doped samples the defect space includes an O^{2-} vacancy and the two nearest-neighbour dopant cations [21] while in a case of Nd-doped samples the defect space can be decomposed to the space with and without an O^{2-} vacancy [13]. On the other hand the F_{2g} mode, whose frequency is attributed to the symmetrical stretching mode of the Ce-O8 vibrational unit, should be very sensitive to any disorder in the oxygen sub-lattice [22]. The increased concentration of oxygen vacancies usually influences the position, shape and width of the Raman line. Bearing in mind the asymmetrical broadening of the F_{2g} mode, from ∼10 to ∼40 cm^{-1} for single crystal and doped nanostructured samples, we assumed that such a broadening of the F_{2g} mode in $Ce_{1-x}Y(Nd)_xO_{2-\delta}$ solid solutions is mainly due to the presence of a high concentration of oxygen vacancies.

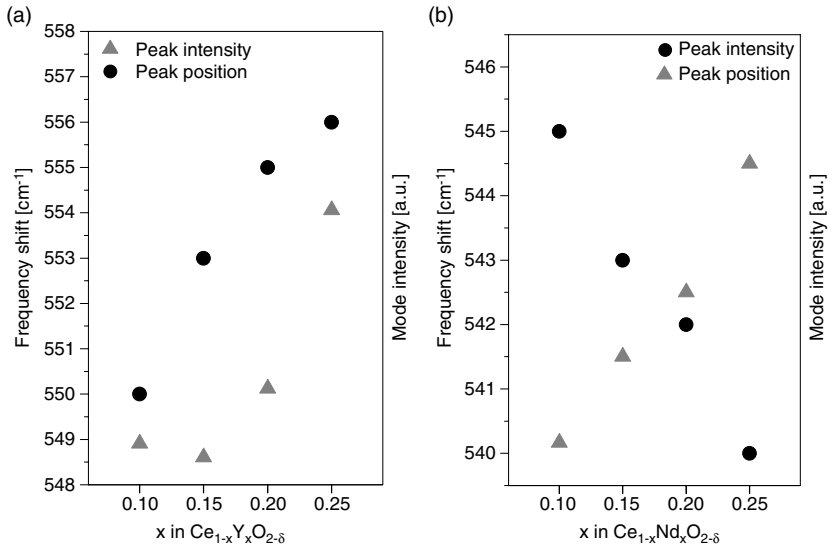

Figure 5. Position and intensity change of the Raman mode, associated with introduced O^{2-} vacancies, with doping fraction for $Ce_{1-x}Y_xO_{2-\delta}$ nanopowders ($0.1 \leqslant x \leqslant 0.25$) (a) and $Ce_{1-x}Nd_xO_{2-\delta}$ nanopowders ($0.1 \leqslant x \leqslant 0.25$) (b).

4. Conclusion

In summary, $Ce_{1-x}Y(Nd)_xO_{2-\delta}$ solid solutions ($0.1 \leqslant x \leqslant 0.25$) with fluorite structure were prepared by the SPRT method. The Raman spectra are described using a spatial correlation model with combined size and inhomogeneous strain effects. It has been found that the Raman spectra are influenced by the defect spaces associated with the oxygen vacancies. These O^{2-} vacancies originate from the non-stoichiometry of ceria nanopowders (intrinsic vacancies) or from the substitution of Ce^{4+} ions with trivalent Y^{3+} and Nd^{3+} cations (extrinsic vacancies). The concentration of extrinsic O^{2-} vacancies increases with doping in both series of samples, probably followed by a change in the type of defect space in Y- and Nd-doped ceria nanopowders. Therefore Raman spectroscopy is a very effective diagnostic method for detecting the presence of oxygen vacancies as well as the dependence of the defect spaces on dopant type.

Acknowledgment

This work was financially supported by the Serbian MSEP under project no 141047.

References

[1] Steel B C H 2000 *Solid State Ion.* **129** 95
[2] Mori T, Drennan J, Lee J H, Li J G and Ikegami T 2002 *Solid State Ion.* **154/155** 461
[3] Herle J V, Horita T, Kawada T, Sakai N, Yokokawa H and Dokiya M 1996 *Solid State Ion.* **86–88** 1255
[4] Yahiro H, Baba Y, Eguchi K and Arai H 1988 *J. Electrochem. Soc.* **135** 2077
[5] Matsui T, Inaba M, Mineshige A and Ogumi Z 2005 *Solid State Ion.* **176** 647
[6] Peng C, Wang Y, Jiang K, Bin B Q, Liang H W, Feng J and Meng J 2003 *J. Alloys Compounds* **349** 273
[7] Bai W, Choy K L, Stelzer N H J and Schoonman J 1999 *Solid State Ion.* **116** 225

[8] Sin A, Dubitsky Y, Zaopo A, Aricò A S, Gullo L, La Rosa D, Siracusano S, Antonucci V, Oliva C and Ballabio O 2004 *Solid State Ion.* **175** 361
[9] Bošković S, Djurović D, Dohčević-Mitrović Z, Popović Z, Zinkevich M and Aldinger F 2005 *J. Power Sources* **145** 237
[10] Tsunekawa S, Sivamohan R, Ito S, Kasuya A and Fukuda T 1999 *Nanostruct. Mater.* **11** 141
[11] Zhou X D and Huebner W 2001 *Appl. Phys. Lett.* **79** 21
[12] Weber W H, Hass K C and McBride J R 1993 *Phys. Rev.* B **48** 178
[13] Nakajima A, Yoshihara A and Ishigame M 1994 *Phys. Rev.* B **50** 13297
[14] Dohčević-Mitrović Z D, Šćepanović M J, Grujić-Brojčin M U, Popović Z V, Bošković S B, Matović B M, Zinkevich M V and Aldinger F 2006 *Solid State Commun.* **137** 387
[15] Richter H, Wang Z P and Ley L 1981 *Solid State Commun.* **39** 625
[16] Campbell I H and Fauchet P M 1986 *Solid State Commun.* **58** 739
[17] Spanier J E, Robinson R D, Zhang F, Chan S W and Herman I P 2001 *Phys. Rev.* B **64** 245407
[18] Hernandez-Alonso M D, Hugria A B, Martinez-Arias A, Coronado J M, Conesa J C, Soria J and Fernandez-Garcia M 2004 *Phys. Chem. Chem. Phys.* **6** 3524
[19] Mcbride J R, Hass K C, Poindexter B D and Weber W H 1994 *J. Appl. Phys.* **76** 2435
[20] Lin X M, Li L P, Li G S and Su W H 2001 *Mater. Chem. Phys.* **69** 236
[21] Anderson M P, Cox D E, Halperin K and Nowick A S 1983 *Solid State Ion.* **9/10** 953
[22] Kosacki I, Suzuki T, Anderson H U and Colomban P 2002 *Solid State Ion.* **149** 99